



A Seasonal Climatology of the Mexico City Atmospheric Boundary Layer

Andrea Burgos-Cuevas¹ · David K. Adams¹ · Jorge Luis García-Franco² · Angel Ruiz-Angulo^{3,4}

Received: 28 August 2020 / Accepted: 6 March 2021 / Published online: 6 April 2021
© The Author(s), under exclusive licence to Springer Nature B.V. 2021

Abstract

Lower tropospheric thermal structure greatly affects atmospheric boundary-layer (ABL) stability and mixing processes with the free troposphere. In particular, in polluted urban zones, ABL stratification becomes a key variable in air quality research. This study focuses on generating a climatology (1990–2017) of the seasonal variability of ABL thermal structure in Mexico City by way of radiosonde analysis. Thermal inversion intensity and frequency are shown to be greater during winter and spring, a behaviour which coincides with greater pollutant concentrations. Higher concentrations are found during the dry season (November to May) than during the rainy months. In addition, significantly higher than normal surface pollutant concentrations are found on days with simple thermal inversion layers as well as during multilayer inversion days. Furthermore, stable layers, determined by potential temperature, are found throughout the year but more frequently during winter, whereas stable layers based on the virtual potential temperature prevail all year. In regions of complex terrain, such multiple stable layers have also been identified by previous authors. Additionally, the most unstable surface layers (in which the bulk Richardson number (Ri_B) is small) develop during the rainy season, whereas during winter there are more levels in the vertical column with higher Ri_B values. Although the Mexico City ABL and pollution episodes have been widely studied, this represents the first long-term investigation to consider the thermal stability of the ABL. Therefore, the present study provides a baseline for further research employing different observational techniques and high-resolution numerical models.

Keywords Air quality · Complex terrain · Multiple stable layers · Seasonal variability · Thermal structure

✉ Andrea Burgos-Cuevas
andreab.app@atmosfera.unam.mx

¹ Centro de Ciencias de la Atmósfera, Universidad Nacional Autónoma de México, Mexico City, Mexico

² Department of Physics, Oxford, UK

³ Institute of Earth Sciences, University of Iceland, Reykjavik, Iceland

⁴ Icelandic Meteorological Office, Reykjavík, Iceland

1 Introduction

The atmospheric boundary layer (ABL) constitutes the lower portion of the troposphere in which the vertical exchange of heat, water vapour as well as tracers, such as aerosols, particulate matter and gaseous pollutants take place (Coulter 1979; Garratt 1994; Stull 2012). It is well established that the ABL, its height and its thermodynamic structure can strongly influence air quality (Guo et al. 2009; Pal and Haefelin 2015; Li et al. 2017; Zhang et al. 2018). In particular, the ABL height is an important parameter in determining the strength of vertical and horizontal transport of pollutants (Haikin et al. 2015; Berkes et al. 2016; Guo et al. 2016). The ABL height has traditionally been determined from vertical profiles of temperature and humidity derived from atmospheric soundings and, more recently, from remote-sensing techniques such as lidar and sodar (Steyn et al. 1999; Hennemuth and Lammert 2006; Zhang et al. 2014; Guo et al. 2016; Zhang et al. 2018). Nevertheless, the height of the ABL is not always easily determined (De Wekker and Kossmann 2015; Herrera-Mejía and Hoyos 2019); it has been shown that, in regions of complex terrain, the ABL vertical structure can become increasingly intricate with multiple stable layers capable of confining pollutants below (Kolev et al. 2000; De Wekker and Kossmann 2015; Largeton and Staquet 2016b; Serafin et al. 2018). There are various physical mechanisms by which stable layers stifle the mixing of pollutants and other tracers. These layers can control whether the valley atmosphere is coupled or decoupled with the overlying free atmosphere where synoptic flow is typically able to ventilate pollutants. Stable layers closer to the ground have been found to control multi-scale interactions which enhance or stifle mixing (Serafin et al. 2018). One of the mechanisms that favours turbulent exchange within the ABL is the breaking of internal gravity waves (Mahrt 1999; Sun et al. 2015). However, stable layers can confine these turbulent motions, thereby impeding vertical mixing and increasing the concentration of near-surface pollutants (Serafin et al. 2018). Hence, for urban zones situated in mountain-valley configurations, further study is required to better characterize multi-stable-layer ABL structure and its impact on pollution events.

The influence of airborne emissions from large urban conglomerations (e.g., megacities) extends far beyond the local area (Molina et al. 2018). For example, urban pollution can determine regional air quality due to contaminant transport. Even global effects arise from megacity emissions given that they are large sources of greenhouse gas emissions (Molina et al. 2010). However, to understand the complex relationship between pollution episodes, meteorological conditions and the urban ABL, long-term observations are critical. More robust observational datasets are needed to improve theory, derive adequate parametrizations of physical processes, as well as to validate numerical model output (Martilli 2007; Barlow 2014).

In the simplest framework, the urban ABL evolution and height are strongly tied to the diurnal cycle of insolation. The convective boundary layer (CBL) generally develops during daytime hours, while a stable surface and residual layer often form overnight (Stull 2012; LeMone et al. 2013, 2014; Zhang et al. 2018). However, the diurnal evolution of the ABL (as well as its structure, dynamical processes, and pollutant concentration) often reveal strong seasonal variability. For instance, the climatological ABL height over Beijing and Shanghai exhibits large seasonal variations, which are associated with changes in aerosol concentrations (Zhang et al. 2018). Similarly, black carbon concentrations in New Delhi (Tiwari et al. 2013) and nitrous oxide (NO) episodes in Los Angeles (Gorham et al. 2010) are also strongly linked to seasonality. The ABL structure also varies subseasonally according to temperature and insolation patterns, as found for Santiago, Chile, in both winter (Ragsdale et al. 2013)

and summer (Barrett et al. 2012). Given the seasonal impact on ABL vertical structure, its characterization is a fundamental goal of air pollution research, and hence requires multi-year datasets (Coulter 1979; Van Pul et al. 1994; Cao et al. 2007; Guo et al. 2016). As noted above, a further confounding factor to seasonality is the effect of complex topography given that mountain-valley circulations can complicate the simple vertical-stability-structure paradigm (Kolev et al. 2000; Haikin et al. 2015).

A particular case in point is Mexico City, where both seasonality and complex topography play fundamental roles in the evolution of ABL vertical structure and pollution episodes. It is worth noting that seasonality exerts different impacts on the ABL; however, diurnal insolation variability is one of the most important drivers determining ABL stable layers and their depth (Zhou et al. 2016; Levi et al. 2020). As one of the world's most populous cities, Mexico City experiences a heavy daily load of emissions from more than four million vehicles, as well as from industry, significantly affecting air quality (Molina et al. 2007; Chavez-Baeza and Sheinbaum-Pardo 2014; Peralta et al. 2019). Contamination transport resulting from local circulations in Mexico City and associated meteorological conditions has been investigated (Doran et al. 1998; Jáuregui 1988; Whiteman et al. 2000; Doran 2007; Molina et al. 2007). Results from these campaign studies have indicated that a close relationship exists between high-pollution episodes and thermal inversions in Mexico City. This implies that, in the presence of thermal inversions, surface air quality is usually poorer when inversions are absent. With respect to seasonality, previous studies have also found that the frequency of surface-based thermal inversions is greatest from November to April, while from May to October enhanced unstable convective conditions provide vertical ventilation favouring pollutant dispersion (Jáuregui 1988; de Foy et al. 2006; Carreón-Sierra et al. 2015). Likewise, the role of complex terrain in generating local circulations may also enhance the trapping of pollutants (Oke et al. 1992; Doran et al. 1998; Jazcilevich et al. 2003). In particular, it has been shown that local circulation patterns, due to the topographically and thermally driven flow, are important in the basin for the transport and diffusion of pollutants (Doran et al. 1998). In addition, the local circulation can become complex because, as shown by Jazcilevich et al. (2003), cold air can be transported upwards due to mechanical advection when air parcels are forced against the mountains, and they then tend to descend at night given they are typically colder than the surrounding air. Nevertheless, as noted above, given the lack of long-term observations adequately covering the complex topographic features, Mexico City-based studies on ABL inversions have been short-term observational/experimental campaigns or modelling studies (Whiteman et al. 2000; Raga et al. 2001; Jazcilevich et al. 2003; de Foy et al. 2006; Molina et al. 2010; Apel et al. 2010).

Although several studies have been carried out on the ABL height structure over Mexico City (e.g., Doran et al. 1998; Whiteman et al. 2000; Velasco et al. 2008), only one longer-term study of the ABL height and its diurnal evolution has been carried out (García-Franco et al. 2018). These authors analyzed nearly six complete years of ceilometer backscatter data providing high-temporal-resolution ABL height observations, permitting the characterization of the ABL height evolution as well as its seasonal variability. Their results revealed that maximum mixed-layer heights (MLHs) occur between 2500 and 3000 m above ground level (a.g.l.). This latter maximum MLH is used here for the purpose of analyzing ABL structure (see Sect. 3). A long-term study relating thermodynamic and dynamic parameters/variables to the ABL internal stratification structure over Mexico City is still lacking and we intend to fill this void.

Taking into account previous ABL research in Mexico City, we focus on the hitherto unexplored seasonal variability of the thermal-stratification structure. Previous authors have pointed out that, in a mountain-valley topographic configuration, such as that of the Valley of

Mexico, the thermal stratification is complex (Kolev et al. 2000; De Wekker and Kossmann 2015; Serafin et al. 2018). In particular, just before sunrise, near-surface airflow over sloping terrain is typically down-valley. Downslope flows enhance the accumulation of cold air in valleys and basins, which contributes to strong stability and tends to hinder the growth of the CBL the next day (De Wekker and Kossmann 2015). This stable layer (associated with the downslope flow), together with the surface inversion layer and any elevated residual inversions, can lead to multiple stable layers that are identified as positive gradients in the potential temperature profiles (De Wekker and Kossmann 2015). Moreover, upslope flow contributes to vertical mixing during the daytime (Adler and Kalthoff 2014). A portion of the pollutants may be transported above the CBL top (De Wekker and Kossmann 2015; Serafin et al. 2018), where they can be re-entrained into the valley CBL due to subsidence over the valley, or vented into the free troposphere (De Wekker and Kossmann 2015). However, stable layers are also able to resist erosion by wind shear, suppress turbulence, inhibit vertical exchange, and affect mixing processes due to gravity-wave breaking. This last effect can take place either by controlling the propagation of gravity-wave modes or by trapping the wave energy in the underlying boundary layer (Serafin et al. 2018). In summary, multiple stable layers affect the mixing mechanisms within the ABL, with implications for air quality in large urban areas in mountain-valley configurations (Nodzu et al. 2006; Serafin et al. 2018). Moreover, these stable layers may also be present during night-time (Kolev et al. 2000). In fact, the nocturnal boundary layer can also have a complex and very variable structure, which makes it difficult to determine its depth (Huang et al. 2017).

The present study focuses on the ABL stratification characteristics in Mexico City, which are also observed in other urban zones of complex mountainous terrain (De Wekker and Kossmann 2015; Serafin et al. 2018; Zhao et al. 2018). Our specific aim is to investigate ABL stratification and its relationship with quantitative measures of local air pollution. To this end, long-term, early-morning atmospheric soundings as well as measurements of six atmospheric pollutants are analyzed on monthly time scales. Specifically, we analyze thermal inversions and stratification structures of stable layers in order to elucidate the relationship between commonly employed atmospheric pollutants used in air quality research (Wang et al. 2014; Zhang et al. 2015) and ABL stability. In what follows, we provide details on the radiosonde and air pollution data used, as well as the methodology for determining stable-layer inversions, their intensity and height, as well as dynamically stable layers. We then present results from monthly mean distributions of inversion layers, followed by a discussion and summary of these results in the context of previous studies.

2 Study Site and Data

Mexico City lies in an elevated valley (≈ 2250 m a.s.l.) with a horizontal extent of approximately 9600 km². The topographic configuration includes several mountain chains and hills which may act to confine contaminants. In the south-western portion of the valley, the Ajusco mountains reach heights of 800 to 1000 m a.g.l.; i.e., above the valley floor. Continuing northwards on the western side of the valley, a chain of mountains rises to 1000 m a.g.l. On the eastern side, snow-capped volcanoes reach more than 3000 m a.g.l. (5.6 km above sea level) (Whiteman et al. 2000). In addition, between Mexico City and this volcanic range lies the Chalco Valley, separated from Mexico City by a line of smaller hills (≈ 200 m a.g.l.) that may also contribute to the local circulation's complexity. The Valley of Mexico opens on the north-east side towards Texcoco lake.

Here, 28 years of radiosonde data (1990–2017) are employed to analyze the vertical stability in the ABL based on thermodynamic variables and a stability parameter (see Sect. 3). Specifically, daily radiosonde data from the Mexican National Weather Service (*Servicio Meteorológico Nacional*, SMN) are available from balloon soundings at 1200 UTC and 0000 UTC which can be downloaded from the University of Wyoming sounding site (<http://weather.uwyo.edu/upperair/sounding.html>). From these sounding data, we consider pressure, temperature, geopotential height, potential temperature (θ), and virtual potential temperature (θ_v), as well as the wind speed and direction. Given our focus on the generally stable, early-morning boundary layer, only 1200 UTC soundings are considered. Soundings were launched at the Mexico City International Airport (19.44° N, 99.07° E) until March 1998. After this date, the launches took place at the Tacubaya Observatory (19.40° N, 99.17° E), ≈ 12 km to the west of the airport. The Tacubaya Observatory lies near the base of the western hills which may influence the ABL vertical structure. To discern possible differences in ABL structure at both locations, we compute the Wilcoxon–Mann–Whitney rank-sum test implemented in MATLAB[®] by month for three parameters. The parameter one is

$$\Gamma_{\max} = \max \left(\frac{\Delta T}{\Delta z} \right), \quad (1)$$

where T is the temperature, and z is the vertical coordinate. The other two statistics are the height at which Γ_{\max} is reached,

$$z_{\max} = z(\Gamma_{\max}), \quad (2)$$

and the mean thermal gradient within the ABL, $\Gamma_{\text{mean}} = \text{mean}(\Delta T / \Delta z)$. The parameters Γ_{\max} and z_{\max} are also employed in Sect. 3.3 in the analysis of monthly ABL stability. These three statistics are generated for data before 1998 (at the airport) and after 1998 (at the Tacubaya Observatory). For each month for the corresponding years at each site, the 1200 UTC daily sounding data are used to calculate monthly p values and corresponding h values. The p value is the specific probability that the observed value of this test statistic occurs according to the null distribution. The h value is $h = 1$ if the null hypothesis (which is that the two samples correspond to the same dataset) is rejected and $h = 0$ otherwise.

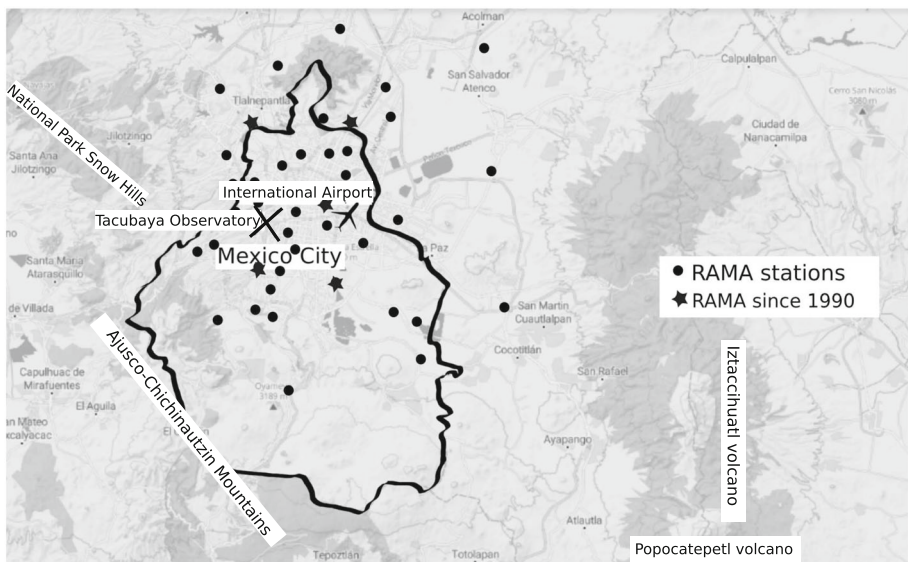
These values are shown in Table 1, where all 12 monthly h values are zero for the parameter Γ_{\max} . Hence, the null hypothesis for this statistical test can not be rejected, implying the monthly distributions at each site correspond to the same dataset. However, the results of applying the Wilcoxon–Mann–Whitney rank-sum test for the parameters z_{\max} and Γ_{mean} differ slightly. In the case of Γ_{\max} , we obtain $h = 0$ for 11 months, whereas for February $h = 1$. Regarding Γ_{mean} , $h = 0$ for 10 months. However, for April and October, the Γ_{mean} results in $h = 1$. Although there are three months where $h = 1$, we are confident that the distributions are essentially the same, given that, for the vast majority of months, $h = 0$. The locations of the two radiosonde sites are shown in Fig. 1.

Typically, each sounding lasts less than 90 min and the data are reported according to World Meteorological Organization standards. The soundings measure vertical profiles of pressure, temperature, humidity, and the wind speed and direction. Based on these variables, the parameters θ and θ_v are estimated as well as the bulk Richardson number in order to identify thermal inversions and stable layers.

In order to link vertical stability structure to local air quality, pollutant concentrations measured from the Automated Atmospheric Monitoring Network (*Red Automática de Monitoreo Atmosférico*, RAMA) are utilized, similarly to previous studies (Raga and Le Moyne 1996; Ortuño et al. 1997; Zhang et al. 2009; Barrett and Raga 2016; García-Franco 2020). Specifically, we examine several primary pollutants such as CO, NO, NO₂ and fine particulate

Table 1 Resulting p and h monthly values for the Wilcoxon–Mann–Whitney rank-sum test for three parameters: Γ_{\max} , z_{\max} , and Γ_{mean}

Month	Γ_{\max}	z_{\max}	Γ_{mean}
Jan	$p = 0.6716$ $h = 0$	$p = 0.0795$ $h = 0$	$p = 0.5042$ $h = 0$
Feb	$p = 0.1849$ $h = 0$	$p = 0.0170$ $h = 1$	$p = 0.3703$ $h = 0$
Mar	$p = 0.6054$ $h = 0$	$p = 0.9367$ $h = 0$	$p = 0.5452$ $h = 0$
Apr	$p = 0.0876$ $h = 0$	$p = 0.3917$ $h = 0$	$p = 0.0241$ $h = 1$
May	$p = 0.0994$ $h = 0$	$p = 0.6549$ $h = 0$	$p = 0.8540$ $h = 0$
Jun	$p = 0.6961$ $h = 0$	$p = 0.3397$ $h = 0$	$p = 0.7769$ $h = 0$
Jul	$p = 0.8111$ $h = 0$	$p = 0.3055$ $h = 0$	$p = 0.4220$ $h = 0$
Aug	$p = 0.9582$ $h = 0$	$p = 0.2304$ $h = 0$	$p = 0.9916$ $h = 0$
Sep	$p = 0.3734$ $h = 0$	$p = 0.0624$ $h = 0$	$p = 0.5979$ $h = 0$
Oct	$p = 0.3812$ $h = 0$	$p = 0.0583$ $h = 0$	$p = 0.0201$ $h = 1$
Nov	$p = 0.8730$ $h = 0$	$p = 0.3883$ $h = 0$	$p = 0.1571$ $h = 0$
Dec	$p = 0.1215$ $h = 0$	$p = 0.3068$ $h = 0$	$p = 0.3251$ $h = 0$

**Fig. 1** Map of the study area revealing the complex topography around the Valley of Mexico. The black line corresponds to the official limits of Mexico City. The systems of mountains, Ajusco-Chichinautzin corridor and the Popocatepetl and Iztaccihuatl volcanoes, are labeled. The locations of the radiosonde at the Mexico City International Airport (1990–1998) and the Tacubaya Observatory (1998–2017) are also indicated. The black dots correspond to the location of the RAMA pollution monitoring stations with variable record lengths, while the stars indicate the stations in which NO and NO₂ were monitored since 1990

matter, PM₁₀ and PM_{2.5}. Ozone (O₃) concentration is also analyzed, though this pollutant is not emitted directly into the atmosphere, but results from photochemical reactions in which the precursors are NO and NO₂; therefore, O₃ is a secondary pollutant. The primary pollutants studied here are associated with fossil fuel combustion (Wang et al. 2001) and are capable of directly affecting human health (Kampa and Castanas 2008). Of particular rel-

evance here, high CO, O₃, particulate matter and NO_x (NO and NO₂) concentrations have been previously associated with atmospheric stability, weaker vertical mixing, and the confinement of pollutants in urban sites around the world (Raga et al. 2001; Wang et al. 2001; Badarinath et al. 2009; Quan et al. 2013). Furthermore, the pollutants CO, NO, NO₂, and O₃ have been measured in Mexico City over our period of interest (1990–2017). In 1990, only a few stations measured these pollutants, whereas by 2017, all contaminants were measured at more than 30 sites. In the case of PM₁₀, it was first monitored in 1995 and, since 2003, PM_{2.5} has also been measured. These pollutant concentrations are reported hourly. Since our focus is on early-morning stability, we examine pollutant concentrations between 0400 LT (local time = UTC - 6 h) and 0800 LT, coincident with the morning sounding, in addition to daily mean concentrations.

3 Methodology

The ABL stability is typically defined based on potential temperature profiles (Kolev et al. 2000; Martucci et al. 2007; Stull 2012). In particular, over Mexico City, these thermal profiles have been used to classify ABL stability and its diurnal evolution (Whiteman et al. 1999, 2000). Here, the monthly variability of inversions and stable layers are identified in terms of thermal profiles. In addition, monthly composites of the maximum inversion intensity Γ_{\max} (Eq. 1), are created. The maximum inversion intensity is a particularly relevant variable because it indicates the most stable layer in the thermal profile within the ABL and, therefore, indicates how strongly vertical movements can be impeded. The parameter z_{\max} is also computed in order to assess the height in the ABL that pollutants reach before the mixing processes are affected by this stable layer. The bulk Richardson number, Ri_B (as utilized also by Velasco et al. 2008; Zhang et al. 2014) can be defined as

$$Ri_B = \frac{g\Delta\theta_v\Delta z}{\theta_v(\Delta U)^2}, \quad (3)$$

where g is the acceleration due to gravity, $\Delta\theta_v$ is the virtual potential temperature difference between the top and bottom of the layer, θ_v corresponds to the virtual potential temperature at the top of the layer, and ΔU is the difference in wind speed across the layer. This definition of Ri_B is also used to account for the influence of wind shear on stability and turbulent mixing processes. Finally, the sounding analysis results serve as the basis for examining pollutant concentrations measured at RAMA stations from 1990 to 2017. Specifically, monthly variability of the stratification structure and associated pollutant concentrations are calculated, thereby tying atmospheric contaminant levels with morning ABL stability profiles.

The effect of the thermal stability of the atmosphere on pollutant concentrations is investigated through the comparison of the composites. The hourly mean pollutant data observed between 0400 LT and 0800 LT from each station is averaged into one daily mean value for the whole RAMA network for the period 1990–2017 (note that the specific period varies for each pollutant as some pollutants were only monitored by the network post-1990). The composites are then split based on the different inversion types for each day and a Welch t -test is used to evaluate the significance of the differences between the inversion types and the climatology.

Vertical sounding structure could certainly be affected by early-morning precipitation. However, hourly precipitation data for the length of our study are not available. Nevertheless, late-night and early-morning precipitation is very unusual for the Valley of Mexico (Jáuregui and Romales 1996; Jáuregui 1997) and, hence, should not affect our analysis.

When analyzing sounding profiles, erroneous data may be included for a variety of reasons. In order to eliminate these data, the soundings underwent quality control (see below). Given the frequent occurrence of erroneous temperature and humidity data at and just above the surface level, measurements between 0 to 50 m a.g.l. are not included here. Furthermore, considering that the diurnal CBL hardly ever reaches 3000 m according to previous authors (Doran et al. 1998; García-Franco et al. 2018), and that the residual layer does not extend much higher than the CBL, we focus on profiles below 2900 m. Within the resulting layer from 50 to 2900 m a.g.l., a detailed analysis is performed. Spurious radiosonde profiles are neglected according to the following criteria:

1. Incomplete profiles: whenever a radiosonde profile does not include continuous vertical information of at least 1.5 km, the profile is disregarded.
2. The available data started above a height of 700 m (a.g.l.): if no data are reported below this threshold height, the profile is not included.
3. Excessive outliers or unrealistic data spikes: a linear regression is fitted to each profile; the fitted variables are T , θ , and θ_v . Whenever the thermal profile diverges from this regression, i.e., the coefficient of determination (R^2) is $R^2 < 0.65$, it is considered physically unrealistic and the profile is neglected.
4. Negative gradients of θ and θ_v : whenever a strong negative gradient, i.e. $\Delta\theta/\Delta z < -1.5 \text{ K km}^{-1}$ or $\Delta\theta_v/\Delta z < -1.5 \text{ K km}^{-1}$, is found, the profile is considered erroneous because of the lack of physical realism.

Utilizing these four criteria for rejection, we eliminate erroneous profiles. For temperature profiles, these criteria result in the elimination of 15% of the soundings. In terms of the θ validation criteria (3 and 4), 17% of the profiles are eliminated. Finally, based on the θ_v criteria (3 and 4), 22% of soundings are disregarded. The remaining soundings considered fall within the height range from 50 to 2900 m. A linear interpolation between the data points is carried out in order to simplify the analysis, following the methodology of Nodzu et al. (2006), and using the *polyfit* MATLAB[®] function between 50 and 2900 m; 100 points for each profile with this interpolation. Profiles are specified for large vertical data gaps are typically neglected given their strong deviation from the linear fit.

The inversion intensity is characterized by using the largest temperature gradient of each profile and monthly composites are created. In addition, z_{\max} (Eq. 2) is identified. Finally, dynamic stability, taking into account the stratification and the wind speed, is investigated utilizing the bulk Richardson number (Sect. 3.4).

3.1 Inversion-Layer Identification (Temperature Criterion)

In general, thermal inversions may be identified when the temperature gradient becomes positive, meaning that whenever the temperature increases with height (z) within a layer, an inversion exists, i.e., $\Delta T/\Delta z > 0$ (Arduini et al. 2016; Largeron and Staquet 2016a). In order to identify multiple inversion layers, when more than one temperature inversion is found, we also count how many positive gradients of temperature there are per profile. Our study considers four different cases:

1. No inversion: $\Delta T/\Delta z \leq 0$ for every z .
2. Simple inversion: $\Delta T/\Delta z > 0$ only once.
3. Two-multilayers: $\Delta T/\Delta z > 0$ twice.
4. Three or more multilayers: $\Delta T/\Delta z > 0$ three or more times.

Examples of these four cases are shown in Fig. 2.

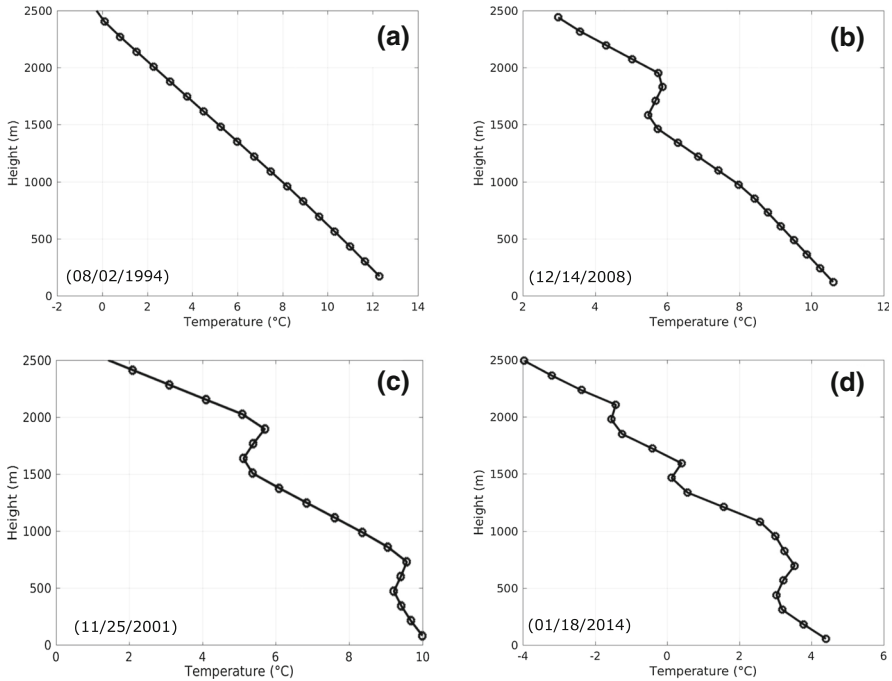


Fig. 2 Typical temperature profile from each inversion type defined in Sect. 3.1: **a** no inversion, **b** simple inversion, **c** two-multilayer inversion, **d** three or more multilayer inversions

3.2 Stable-Layer Identification (θ and θ_v Criteria)

Although the strict definition of a thermal inversion is given in terms of the vertical temperature gradient, to gauge whether a layer is statically stable or unstable to vertical adiabatic motions implies comparing the gradient directly with the dry adiabatic lapse rate. Therefore, other variables, such as θ and θ_v , become more useful in the study of vertical motions given they are conserved under certain assumptions (Nodzu et al. 2006). Furthermore, stable layers (in which $\Delta\theta/\Delta z > 0$ or $\Delta\theta_v/\Delta z > 0$) can suppress convective activity even if $\Delta T/\Delta z > 0$ is not met (Whiteman et al. 1999; Nodzu et al. 2006). The appearance of such stable layers can be deduced from

$$\frac{T}{\theta} \frac{\partial \theta}{\partial z} = \Gamma_d - \Gamma = \Gamma_d + \frac{\partial T}{\partial z}, \tag{4}$$

where $\Gamma_d = g/c_p = 9.8 \text{ K km}^{-1}$, and c_p is the specific heat at constant pressure. Given Eq. 4, whenever in a given layer $\Delta T/\Delta z < 0$ but $0 < |\Delta T/\Delta z| < 9.8 \text{ K km}^{-1}$, that layer is considered statically stable, and not a true inversion. In contrast, if the potential temperature gradient exceeds that of an isothermal atmosphere ($\Delta\theta/\Delta z > 9.8 \text{ K km}^{-1}$), then a true temperature inversion is present; i.e., $\Delta T/\Delta z > 0 \text{ K km}^{-1}$ (Whiteman et al. 1999). However, previous authors have used positive values of $\Delta\theta/\Delta z$ coinciding with a minimum in humidity to identify inversion layers (Martucci et al. 2007). A similar analysis, regarding the effects of humid, but unsaturated, air can be made in terms of θ_v . In this case, we consider the impact of temperature, pressure, and humidity on air density, and its stratification. The

procedure followed for the virtual potential temperature θ_v to identify inversion layers is analogous to the θ case.

Here, true inversion layers, for which $\Delta T/\Delta z > 0$, are identified by employing the temperature criteria. However, the θ and θ_v criteria are instead used to determine ABL stability. Since stable layers, in which the magnitude of $\Delta\theta/\Delta z$ is very small ($\Delta\theta/\Delta z \approx 1 \text{ K km}^{-1}$), can hardly be stable enough to prevent convective activity, a larger specific threshold value is defined. To investigate the stability structure in the ABL, we consider the mean gradient of θ through the ABL from 50 to 2900 m, $(\overline{\Delta\theta/\Delta z})$. If this gradient is below the determined threshold value, the profile is considered to be weakly stable. In this case, inversion layers rarely appear. If there are no values of $\Delta\theta/\Delta z > 6 \text{ K km}^{-1}$ in the profile, the layer is then considered inversion free. In contrast, whenever the mean gradient exceeds the threshold value, a specification of the type of the inversion layer(s) is made. This threshold value is established after analyzing several θ profiles and noting similar values (between 1 and 16 K km^{-1}) reported for the Colorado Plateau by Whiteman et al. (1999). Nonetheless, since we are taking into account the entire profile, our threshold may not be as large as in other studies where shallower inversion layers are considered (Largeron and Staquet 2016a). Though a bit arbitrary, we set the threshold as 2.5 K km^{-1} and then compare this threshold to the mean gradient of the profile, i.e., $\overline{\Delta\theta/\Delta z}$. With this procedure, we classify stable and neutrally stable profiles in four groups:

1. No inversion: $\overline{\Delta\theta/\Delta z} \leq 2.5 \text{ K km}^{-1}$ and $\Delta\theta/\Delta z < 6 \text{ K km}^{-1}$ for every z .
2. Simple inversion: $\overline{\Delta\theta/\Delta z} > 2.5 \text{ K km}^{-1}$ and there is a single localized layer in which $\Delta\theta/\Delta z$ increases significantly.
3. Continuous inversion: $\overline{\Delta\theta/\Delta z} > 3.5 \text{ K km}^{-1}$. In this case, no sharp increment $\Delta\theta/\Delta z$ is found; therefore, the thermal profile may not show a clear inversion layer. However, a large and positive potential temperature gradient can suppress convective activity and, in order to compensate for the lack of a clear temperature inversion layer, the threshold value is considered to be 1 K km^{-1} larger in this case than in the rest of the profiles with sharp inversion layers.
4. Multilayer inversion: $\overline{\Delta\theta/\Delta z} > 2.5 \text{ K km}^{-1}$ and there are two or more localized layers in which $\Delta\theta/\Delta z$ increases significantly.

These four cases of different stable layers according to the θ and θ_v criteria are shown in Fig. 3. Specifically, Fig. 3d corresponds to a multilayer profile for both θ and θ_v classifications. The monthly mean variability of stable layers with these two criteria is shown to be large in Sect. 4. However, in order to clarify the stratification-classification structures, we provide a profile that exhibits a multilayer structure for the both θ and θ_v profiles, Fig. 3d.

3.3 Maximum Inversion Intensity (Γ_{\max})

Different mechanisms can be responsible for stifling vertical mixing between the remnant nocturnal and early-morning ABL and the free troposphere. Therefore, we not only study the stratification structure of the ABL, but also the inversion intensity and its monthly variability. For this purpose, the largest temperature gradient is identified for each vertical profile. Monthly averages are then calculated, considering soundings from 1990 to 2017 and the mean monthly variability of Γ_{\max} (Eq. 1) is presented. This monthly variability of Γ_{\max} complements the inversion structure explained in Sect. 3.2. Furthermore, z_{\max} is also computed and analyzed seasonally. The monthly variability of both the inversion structure, strength, and height are analyzed for determining those months when air quality tends to be poorest.

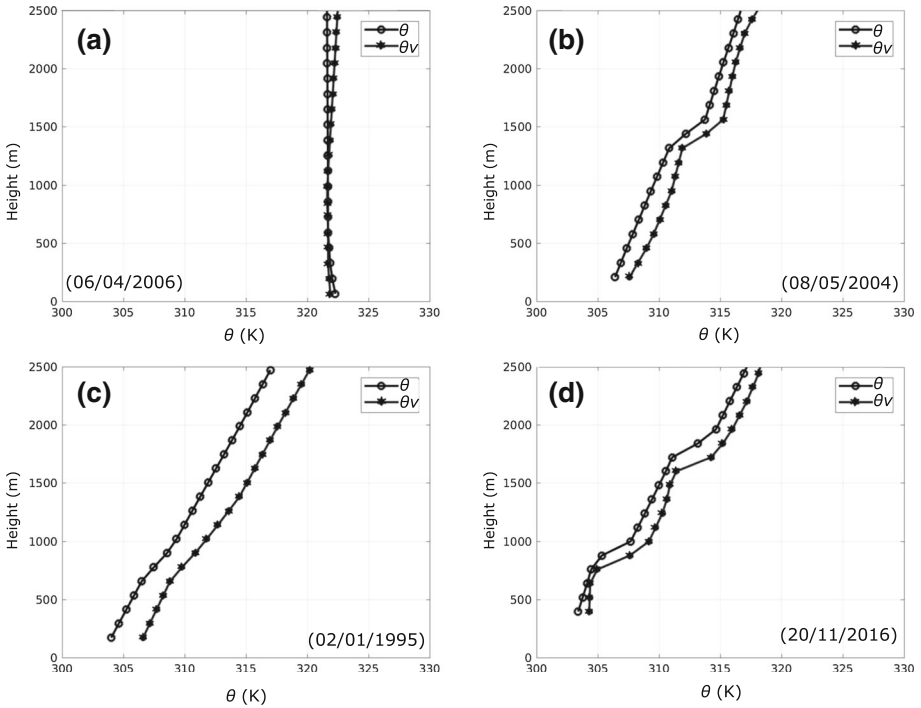


Fig. 3 Vertical θ (circles) and θ_v (dots with crosses) profiles corresponding to each of the stable layers described in Sect. 3.2: **a** no inversion, **b** simple inversion, **c** two continuous inversions, **d** multilayer inversions

3.4 Bulk Richardson Number (Ri_B)

Identifying stable or unstable conditions in the ABL can be accomplished by the use of the bulk Richardson number (Ri_B) (Hansen 1966; Velasco et al. 2008). This dimensionless number is a key parameter in the estimation of the ABL height in numerical-weather-prediction and climate models (Zhang et al. 2014). As the magnitude of Ri_B has been shown to correlate strongly with the air quality (Velasco et al. 2008; Levi et al. 2020), its variability is of interest here. The bulk Richardson number, unlike the gradient Richardson number ($Ri_{grad} = g/\rho(\partial\rho/\partial z)/(\partial U/\partial z)^2$, where ρ is the density of the fluid), is calculated over layers of finite depth Δz . We estimate Ri_B according to Eq. 3, from which it can be seen that larger values of Ri_B are associated with increased layer stability. For the gradient Richardson number, it is clear that if $Ri_{grad} > 0$, then stable conditions prevail, due to strong stratification and weak shear. In contrast, there is no specific threshold for the value of Ri_B above which stable conditions are established. However, some authors have used subjective values derived from lidar data (Cooper and Eichinger 1994), finding that for $Ri_B > 15$, mechanical turbulence becomes negligible and the thermal stratification diminishes buoyant turbulent transport.

We find that the value of Ri_B is sensitive to the layer depth considered, though this value varies in the literature. Given our Ri_B values for a 150-m layer has similar values to those found in Cooper and Eichinger (1994), we adopt their critical value. Since we focus on Ri_B variability throughout the year and at different atmospheric heights, we calculate a normalized Ri_B by dividing the value of Ri_B into its maximum monthly mean value of the entire 28-year

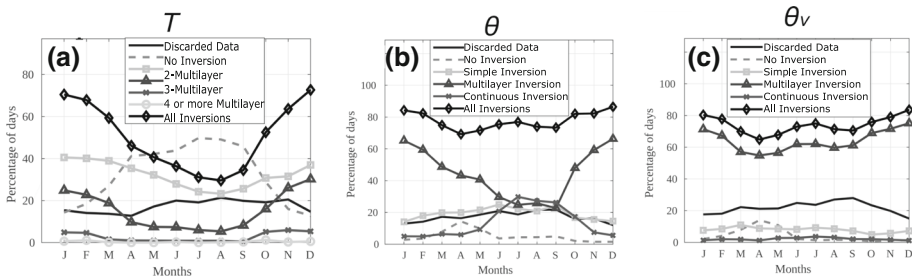


Fig. 4 Monthly variability of the inversion frequencies based on the **a** temperature criterion, **b** potential temperature criterion and **c** virtual potential temperature criterion. For each, different lines correspond to the proposed classification based on stratification complexity

time period. In this manner, we are able to identify the tendency of Ri_B throughout the year, keeping in mind that the larger the value of Ri_B , the more thermal stratification dominates over shear.

The bulk Richardson number is calculated for every θ_v profile at 0600 LT for 20 sounding levels (i.e., each 150 m thick) for all 28 years (1990–2017). The levels, corresponding to the Δz value in Eq. 3 and its corresponding magnitudes of $\Delta\theta_v$ and ΔU , are defined between 50 and 2900 m.

In order to summarize the resulting three-dimensional matrix ($Ri_B \times \text{height} \times \text{day}$) of Ri_B values, we present the value of Ri_B in grayscale. In a similar manner, previous authors have analyzed the vertical distribution of meteorological parameters, including Ri_B (Velasco et al. 2008), to demonstrate at what time of the day the maximum rate of growth of the CBL occurs. Unlike Velasco et al. (2008), we calculate monthly, not diurnal, variability throughout the ABL depth, with the plots presented here composed of monthly averages for the 28-year study period.

4 Results

4.1 Inversion and Stable-Layer Identification and Variability

Once the inversion and stable layers are identified with the criteria based on the parameters T , θ , and θ_v , their monthly variability is presented as in Jáuregui (1988), showing the monthly mean frequencies from 1990 to 2017 as shown in Fig. 4. It can be seen that, according to the temperature criterion, the months with the greatest inversion frequencies are from October to March, while from April to September, lower inversion frequencies are found. This is similar to the result presented by Jáuregui (1988), who found the greatest inversion frequencies from November to April. In contrast, when applying the θ and θ_v criteria, the frequency of stable layers differs: high frequencies of stable layers are found throughout the year, showing a slight decrease in March, April and May.

Regarding the classification of inversion layers according to the temperature criterion, simple inversions prevail as the most frequent inversion type during all months, accounting for 25 to 45% of the days. Multilayers of two inversions are also found, but they only amount for 20 to 30% of the days in the winter months and are less frequent the rest of the year. However, it is worth noting that, during the dry months, which have larger incidences of pollution days, multiple inversion layers develop with a considerably higher frequency. In

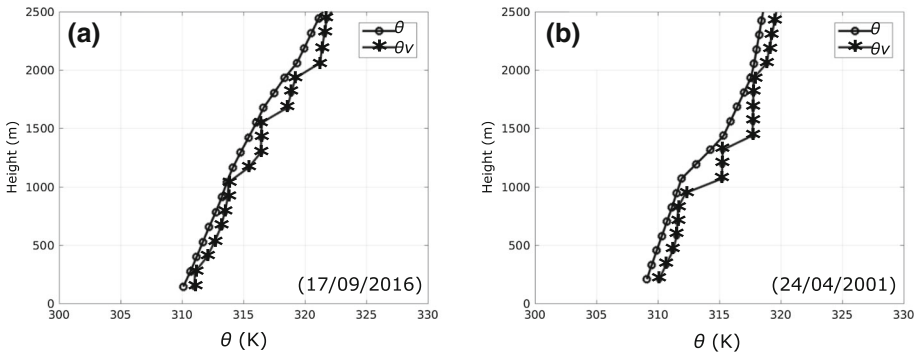


Fig. 5 Potential temperature (circles) and virtual potential temperature (crosses) profiles are shown for two days. **a** The θ profile shows a continuous inversion whereas the θ_v profile has multiple layers of inversions. **b** Although two inversion layers are found in the θ profile, more multilayers (four) develop in the θ_v profile

contrast, with the θ criterion, multilayers prevail as the most frequent inversion type most parts of the year. These types of inversions are present between 30 and 60% of the days from October to June. However, during July, August and September, which are humid and convectively active months, multilayers are less frequent (20–30%) and continuous inversions become the most common stable-layer type. Finally, for the θ_v classification, multilayers are the most frequent inversion type throughout the year. In this case, very few other inversion types are identified: almost no continuous inversions are found and the simple inversions occur in only around 10% of the days. This different behaviour between the θ and the θ_v criteria made us question whether multiple inversion layers can actually be found in many θ_v profiles in which the θ profile does not show multilayers. A further analysis of these cases is carried out and confirms that there are profiles in which the θ_v criterion exhibits multilayers, but the θ criterion does not. Examples are shown in Fig. 5. The more frequent appearance of multilayers with the θ_v criterion than with that based on θ suggests that the humidity may significantly affect stratification. The humidity enhancement of stable layers has already been described, such as by Naakka et al. (2018) who found this in the presumably very different Arctic atmosphere. Although, in the particular case of our study, the θ and θ_v analyzes are unable to elucidate the physical mechanisms that produce more stable layers with the θ_v criterion, it appears that humidity does play an important role in the ABL stability over Mexico City.

4.2 Maximum Inversion Intensity (Γ_{\max})

The seasonal variability of the maximum inversion intensity, as well as the mean monthly composites of Γ_{\max} as well as its height, z_{\max} , are presented in Fig. 6. Although the standard deviation is found to be large because of the presence of extreme Γ_{\max} values ($\Gamma_{\max} < 2 \text{ K km}^{-1}$ and $\Gamma_{\max} > 14 \text{ K km}^{-1}$) all year, the tendency is clear: the largest Γ_{\max} values are found during dry months with scarce rainfall (October to March), whereas during more rainy months (from June to August) the mean Γ_{\max} values are smallest. In April, May and September, intermediate Γ_{\max} values are reached; these months may be considered as transitional.

The seasonal variability of z_{\max} is shown in Fig. 6b, where z_{\max} is found to be relatively constant all year (at around 1500 m). However, April is the one month when this height remains lower than during the rest of the year. Additionally, in May, z_{\max} remains lower

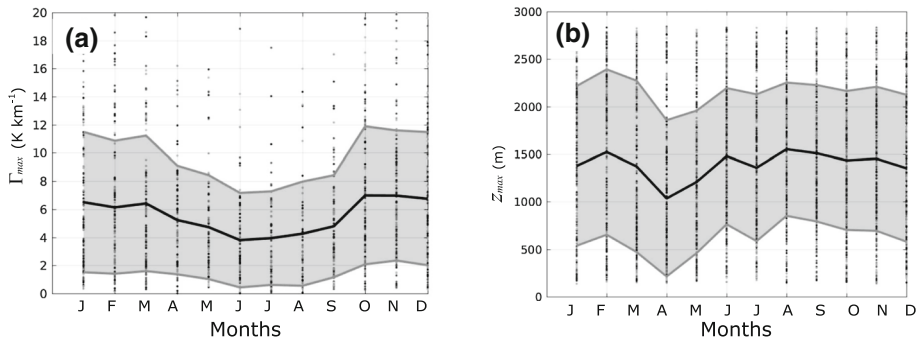


Fig. 6 Mean monthly variability (continuous contour) and standard deviation (grey shadow) of **a** the maximum-inversion intensity and **b** z_{max} from 1990 to 2017. The maximum-inversion intensity is estimated from Eq. 1 considering the temperature of radiosonde profiles at 0600 LT. The dots correspond to the individual data

than the rest of the year, showing that, unlike the maximum-inversion intensity that reaches the largest values during winter, z_{max} does not have this coincident behaviour with the more anticyclonically dominated regime (Jáuregui 1988). However, the fact that z_{max} decreases in April and May is further analyzed and presented in Sects. 4.3 and 4.4.

4.3 Bulk Richardson Number

The estimates of the normalized bulk Richardson number over the 20 defined levels in every θ_v profile yield a three-dimensional matrix: height, month and Ri_B , which is presented in Fig. 7, where we only show the mean of the analyzed years (1990–2017).

The vertical distributions of the normalized Ri_B values in Fig. 7 show that, in the lowest levels, larger bulk Richardson numbers are usually found during the dry months (November to April). These large values indicate that stable stratification dominates over shear, thus inducing the stability conditions capable of inhibiting mixing processes. The occurrence of this stable behaviour can be associated with months where anticyclonic weather dominates, resulting in poor air quality. In contrast, from May to October (warm rainy months), high values of Ri_B are also detected, but they are more confined to specific levels such as $z = 0.9$ km, rather than covering the entire vertical profile. Furthermore, regarding the lower levels ($z < 0.5$ km), the smallest Ri_B values appear from June to October. Nevertheless, very low Ri_B values are also present at higher elevations during spring, especially in April, implying that very unstable layers, with strong shear and weak stratification, develop at higher levels ($1 \text{ km} < z < 2 \text{ km}$) during spring. Perhaps unexpectedly, it has been shown that days with remarkably poor air quality can be associated with the strongest vertical wind direction shear, precisely during the spring months in Mexico City (Molina et al. 2010), which coincide with small Ri_B values.

4.4 Pollutant Concentrations

Regarding the concentrations of CO, NO, NO₂, PM₁₀, PM_{2.5} and O₃, monthly composites are created based on the mean concentration from 0400 LT to 0800 LT at all stations available from 1990 to 2017. Also, mean values taking into account the entire day are calculated. In Fig. 8, a clear tendency of higher levels for all pollutants can be seen during colder months

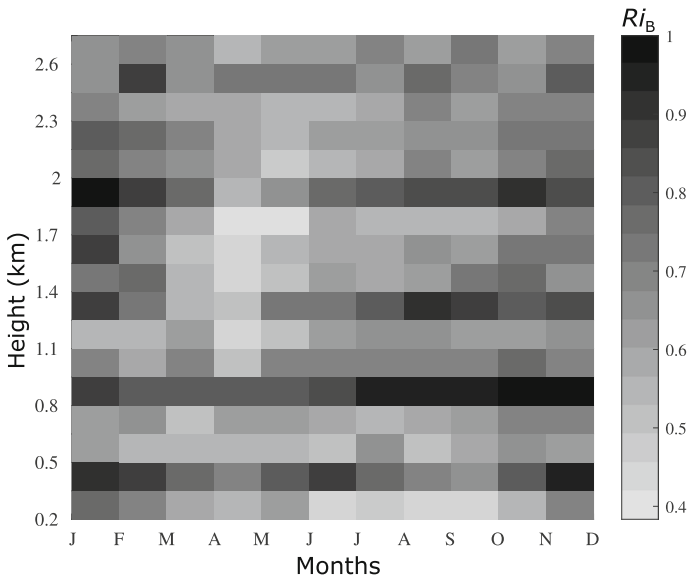


Fig. 7 Vertical distribution of the normalized Ri_B values throughout the year. A mean monthly value is obtained from 1990 to 2017. The darker colours correspond to large Ri_B values that indicate stable layers, whereas the brighter colours infer low Ri_B values and therefore weak stability

with the exception of O_3 . This last contaminant (O_3) is the product of photochemical reactions and its higher values are precisely met during the months with greater insolation (March, April and May). Furthermore, its highest values are reached later in the day and certainly not from 0400 to 0800 LT, given no or very weak insolation. For the rest of the pollutants, the larger concentration levels from November to May are evident both for the daily mean and for the mean in the period 0400 to 0800 LT. However, it can be seen that, during April and May, the mean concentrations from 0400 LT to 0800 LT exceed the daily mean in the cases of CO, NO, NO_2 and $PM_{2.5}$, which demonstrates that the poorest air quality is reached during these early-morning hours. In addition, the pollutant concentration in April and May becomes significantly larger than during the previous and subsequent months (March and June).

In order to relate the concentration tendency of these pollutants with the stratification structure of the early-morning boundary layer, we perform two analyses. We first qualitatively compare the monthly pollutant concentrations of Fig. 8 with the thermal-stratification characteristics shown in Figs. 4, 6 and 7. We note that there is a consistent behaviour between large pollutant concentrations and the frequency of thermal inversions (Fig. 4a). In addition, the inversion intensity (Fig. 6) is also coincidentally larger during the dry cold months in which CO, NO, NO_2 , PM_{10} and $PM_{2.5}$ concentrations also rise. Since multiple stable layers develop all year at a high frequency (Fig. 4b and c), there does not seem to be a relationship between stable layers with the θ and θ_v criteria and the concentration of pollutants. However, we should point out that the frequency of multiple stable layers (θ and θ_v criteria) decreases in April and May with respect to March and June; this occurs with the increase in pollutants during these same months. Finally, z_{max} (Fig. 1b) decreases in April, whereas the pollutant concentrations increase. Therefore, it seems plausible to relate large concentrations of the pollutant with the appearance of a very stable layer at lower heights in the temperature profile.

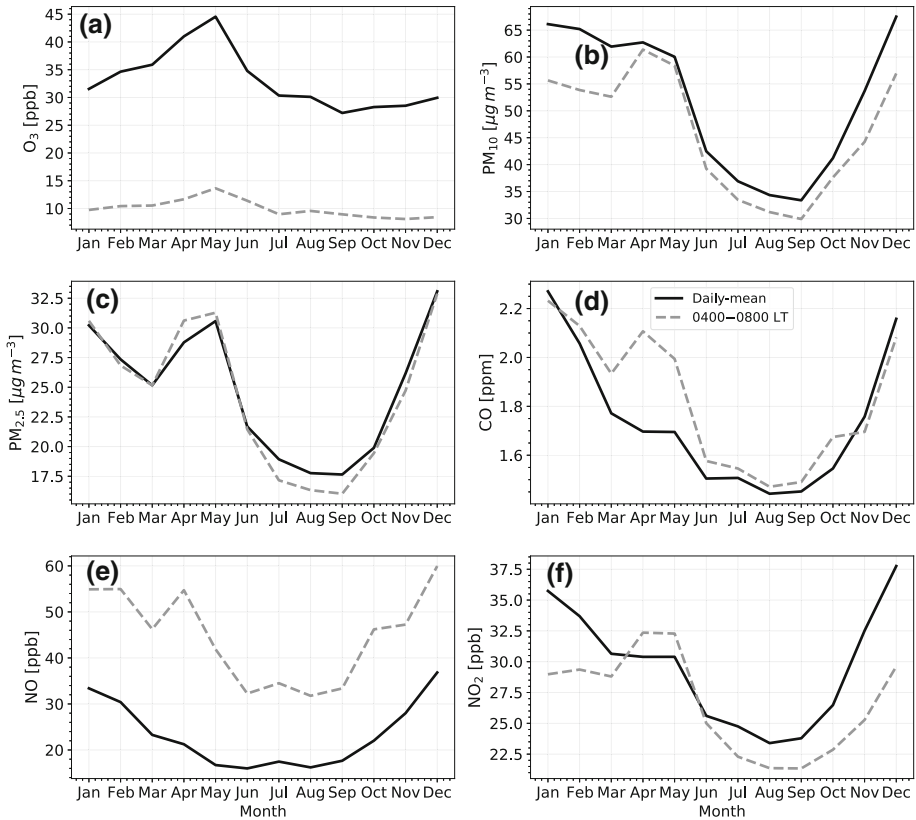


Fig. 8 Monthly mean values of **a** ozone, **b** PM₁₀, **c** PM_{2.5}, **d** CO, **e** NO and **f** NO₂. Results are shown for daily means and mean values between 0400 to 0800 LT for the period 1990–2017, using all available stations of the RAMA network (<http://www.aire.cdmx.gob.mx/>)

Table 2 (upper) Climatological mean values of daily averaged concentrations measured in the 0400 to 0800 LT period and (lower) differences between the composite daily mean and the concentration during each type of inversion

	CO (ppm)	NO (ppb)	NO ₂ (ppb)	PM ₁₀ (µg/m ³)	PM _{2.5} (µg/m ³)	O ₃ (ppb)
Climatology	1.990	45.0	27.2	46.6	24.5	11.5
No Inversion	-0.027	-2.63	-0.91	-3.67	-1.82	+0.30
Simple Inversion	+0.073	+4.92	+1.06	+3.18	+1.01	-0.32
Two multilayer	+0.109	+5.95	+0.98	+5.5	+3.18	-0.56

The differences between each composite sample of the inversion type and the climatological sample that are statistically significant to the 99% confidence interval are shown in bold, according to a Welch *t*-test

A corresponding quantitative analysis is also carried out to relate the thermal inversion types to surface concentrations of pollutants. Table 2 shows the mean pollutant composites based on the inversion-type classification for six pollutants. A climatology of pollutant concentrations is made for the period 1990–2017 and the differences between each composite sample of the inversion type and the climatological sample are shown. In this case, all the days

with two or more inversions are included in the same composite, labelled as two-multilayer. Pollutant concentrations for days with no inversion are found to be lower than normal for all the pollutants, except for O_3 . These lower than normal values are statistically significant for the pollutants NO , NO_2 , PM_{10} , and $PM_{2.5}$, which indicates improved air quality. In contrast, days in which simple inversions appear show significant positive differences for all pollutants except O_3 , which is indicative of higher than normal pollution levels.

Furthermore, days with multilayer profiles also show significantly higher than normal pollutant levels, except for O_3 , and in most cases these differences are higher than the simple inversion case. In order to compare the concentration of pollutants between different types of inversions, we note that the positive values for all the contaminants (except for NO_2) are larger for two multilayer days than for days with simple inversions. This suggests that these multilayers may have a stronger effect on air quality than simple inversions.

In addition, Fig. 9 shows the monthly mean pollutant concentration composites by month at the period from 0400 LT to 0800 LT, i.e., around the morning sounding time. For PM_{10} and $PM_{2.5}$, the monthly mean values do not show a consistent difference between inversion types during the first months of the year. However, after June, the mean PM_{10} and $PM_{2.5}$ concentrations for days without an inversion are found below the levels of simple inversion days and this behaviour continues until the end of the year. For the remaining pollutant concentrations of interest, there is generally no clear-cut, consistent difference between inversion types. However, there are lower than normal levels of NO_2 on days without an inversion during the period from September to December than days with simple inversions.

4.5 Summary

In order to summarize the relationship between ABL structure and pollutant concentration throughout the year, we present Table 3. The monthly variability of temperature inversions is coincident with the two main regimes in Mexico City: the dry cold season with anticyclonic weather bears more frequent thermal inversions, whereas during the warm rainy months, convection is enhanced and thermal inversions become less frequent. The pollutant concentrations roughly coincide with this expected behaviour considering the thermal-inversion variability: large concentrations during the dry season and lower concentrations on the rainy warm months. Nevertheless, a peak of larger concentrations appears during April and May for almost every contaminant. This peak becomes even larger for the pollutant concentrations between 0400 LT and 0800 LT (dashed lines in Fig. 8) than for the daily mean (solid lines in Fig. 8). This peak shows that the concentrations of CO , NO and NO_2 are higher during these hours of the day due to the high emissions of the morning rush-hour traffic and the minimum in MLH before sunrise, in accordance with previous reports of the daily cycle of pollutants and the MLH (Velasco et al. 2008; De Foy et al. 2009; Retama et al. 2015; García-Franco et al. 2018; García-Franco 2020). This rise in pollutant concentrations during April and May is neither associated with a larger inversion frequency (Fig. 4a) nor with more intense inversions (Fig. 6). Regarding the value of Ri_B , it can be seen that, during April and May, there are layers (between 1 and 2 km) in which shear dominates over stratification. These localized layers are not present during the rest of the year, so they may be related to the peak of pollutant concentrations that occur precisely during those months. In addition, z_{max} does not vary significantly the rest of the year, but has a sharp decrease in April and May (Fig. 6). It appears that, during these months, when the frequency and strength of inversions do not enhance the confinement of pollutants, it is the height z_{max} that has an impact on pollutant concentration. This becomes particularly evident between 0400 LT, and 0800 LT

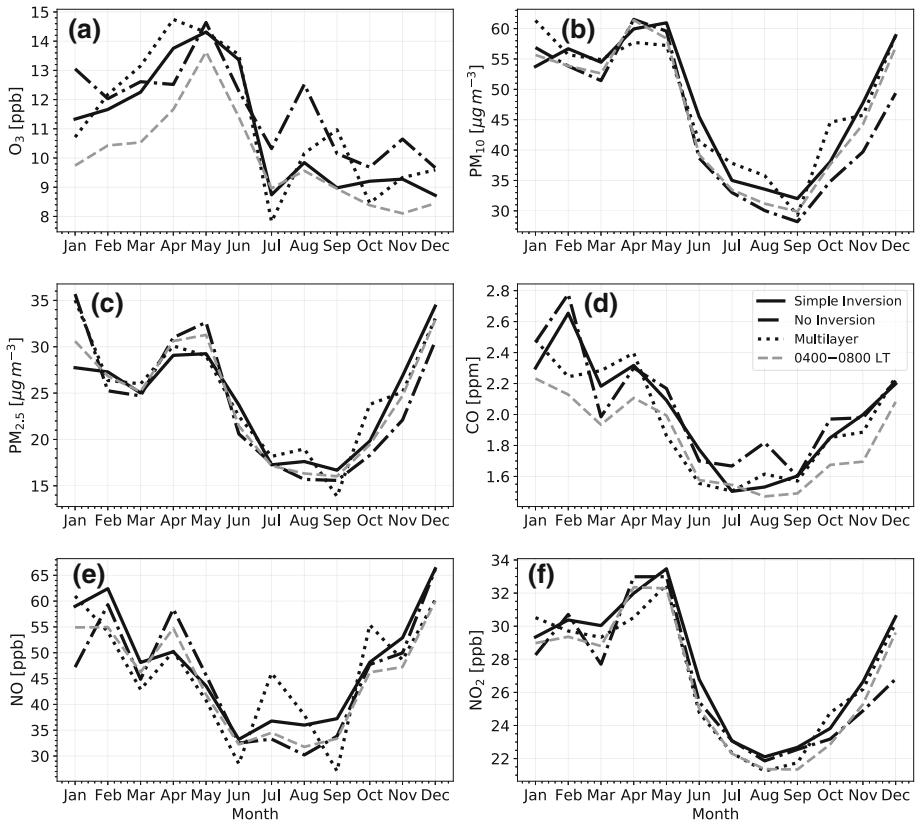


Fig. 9 As in Fig. 8, but also showing the monthly means of days separated into composites of days classified as no inversion, simple inversion, multilayer (two or more) inversions according to the temperature criteria. In all cases, the monthly means are calculated for pollutant concentrations measured only during the 0400 LT to 0800 LT period

during April and May. These months can be considered transitional between the dry cold season and the warm rainy one; they are warm but rain is scarce. This analysis is summarized in Table 3, which covers the main results from Figs. 6, 7, and 8.

5 Conclusions

A long-term characterization of the ABL over Mexico City is carried out with radiosonde data for 28 years (1990–2017) to determine the ABL stratification characteristics associated with the poorest air quality. We focus on vertical profiles from 50 to 2900 m, and analyze the monthly variability of mainly three variables: inversions and stable layers (T , θ , and θ_v criteria), maximum inversion intensity (Γ_{\max}), and the normalized bulk Richardson number (Ri_B). To the best of our knowledge, such a long-term description of the complex stratification structure of the ABL for this region has not been reported previously in the literature.

Monthly frequencies of inversions and stable layers are compared with those frequencies presented by Jáuregui (1988). The annual cycle of the frequency of inversions classified

Table 3 Summary of results regarding the monthly means of Γ_{\max} , its height z_{\max} , Ri_B and the concentrations of pollutants

	Γ_{\max} [K km ⁻¹]	z_{\max} [m]	Ri_B $h(\Gamma_{\max})$	CO [ppm]	NO [ppb]	NO ₂ [ppb]	PM ₁₀ [$\mu\text{g m}^{-3}$]	PM _{2.5} [$\mu\text{g m}^{-3}$]	O ₃ [ppb]
J	6.5	1377	0.9	2.3 2.3	31.7 53.0	35.4 29.0	65.0 54.6	29.7 29.8	31.4 9.8
F	6.1	1522	0.7	2.1 2.2	28.9 53.3	33.1 29.2	63.6 52.4	26.7 25.9	34.5 10.4
M	6.4	1371	0.6	1.9 2.0	22.2 44.9	30.3 28.9	60.9 51.6	25.0 24.9	35.9 10.7
A	5.2	1035	0.5	1.8 2.1	20.0 51.9	30.0 32.4	61.6 59.9	28.7 30.1	41.3 12.1
M	4.7	1280	0.5	1.8 2.0	15.9 40.5	29.9 32.2	59.1 57.3	30.6 31.2	44.6 13.9
J	3.8	1479	0.6	1.6 1.6	15.6 31.6	25.6 25.0	41.9 38.6	21.4 21.0	34.7 11.5
J	3.9	1357	0.6	1.6 1.6	17.1 34.2	24.7 22.4	37.0 33.6	19.0 17.2	30.6 9.2
A	4.2	1552	0.6	1.6 1.5	15.8 31.2	23.5 21.5	34.0 30.7	17.7 16.2	30.3 9.8
S	4.8	1510	0.7	1.6 1.6	17.3 32.9	23.9 21.5	33.3 29.7	17.8 16.1	27.6 9.2
O	7.0	1433	0.8	1.7 1.8	21.5 45.3	26.5 22.9	40.5 36.9	19.6 19.0	28.3 8.5
N	7.0	1451	0.8	1.9 1.8	27.6 46.9	32.7 25.4	53.3 44.0	26.0 24.6	28.8 8.4
D	6.7	1351	0.9	2.4 2.3	35.9 58.9	37.7 29.6	66.9 56.5	32.9 32.6	30.4 8.7

The values of Ri_B shown here correspond to z_{\max} . The CO, NO, NO₂, PM₁₀, PM_{2.5}, and O₃ concentrations are based on the daily mean values, while and after the bars “||”, on the mean values from 0400 LT to 0800 LT

through the temperature profiles is similar to the one presented by Jáuregui for 1981: the largest inversion frequencies are found from October to April (months that have scarce rain), which roughly coincides with poor air quality episodes. This is demonstrated with monthly composites of CO, NO, NO₂, PM₁₀, PM_{2.5}, and O₃ concentrations considering all the available stations in Mexico City from 1990 to 2017, which show larger concentrations from November to May than from June to October. In addition, simple inversions are the most frequent.

In order to relate the inversion type to the concentration of pollutants, a statistical analysis is performed. We found significantly higher than normal contaminant levels on days with simple and multilayer inversions. During days with those two kinds of thermal inversions, the concentrations of CO, NO, NO₂, PM₁₀, and PM_{2.5} show positive values with respect to the climatology (1990–2017), indicating worse than normal air quality. In contrast, on days with no inversion, lower than normal values are found for all pollutants. These findings represent the first climatological study of inversion-layer frequency and type in the ABL over Mexico City. Our approach and results from this long-term sounding analysis provide baseline data and metrics for numerical models, particularly numerical weather prediction models, to assess their realism.

When employing the potential temperature and virtual potential temperature criteria, high frequencies of stable layers are found throughout the year, showing a slight decrease in March, April, May, August, and September. With the θ criterion, multiple stable layers are found on more than 40% of the days during the cold dry months and this frequency decreased for the summer rainy season. Moreover, for the θ_v criterion, multiple stable layers develop on 50 to 80% of days, whereas simple stable layers hardly reached 10%. Although we cannot assess the dynamical linking of multiple stable layers with the local circulation on the Valley of Mexico, we mention that similar complex multilayer ABLs have been reported in the mountainous terrains of other cities (Kolev et al. 2000; Henne et al. 2004; De Wekker and Kossmann 2015; Haikin et al. 2015). However, the presence of multilayer inversions is not found to be coincident with the worst air quality periods (November to May, see Fig. 8), so it appears that these layers are not associated with the confinement of pollutants. Further research regarding this multilayer structure needs to be carried out in order to elucidate the effects that these stable layers may have on the dynamical processes inside the ABL. At present, a network of meteorological sites with sufficient density covering the complex topography of the region does not exist to address possible mechanisms responsible for inversion behaviour. However, local high resolution modelling could employ our results to ascertain the accuracy of their model.

Regarding the variability of the maximum inversion intensity (Γ_{\max}) throughout the year, we find a clear tendency: Γ_{\max} reaches the largest values during the dry cold months and the smallest values during the summer rainy season. Furthermore, intermediate values are present during transitional months such as April and May (dry warm season). This behaviour of Γ_{\max} is also coincident with the period that has the poorest air quality, as can be seen from the larger pollutant concentrations from November to May in Fig. 8. This suggests that the inversion intensity does play an important role in the confinement of pollutants. In contrast, z_{\max} is found to remain relatively constant all year long, with the exception of during April and May. During these transitional months, z_{\max} is found to decrease. This behaviour seems to have a particular effect on the pollutant concentrations, because they tend to increase precisely in April and May. Given that these larger concentrations are neither coincident with a greater temperature-inversion frequency nor with the maximum inversion intensity (Γ_{\max}), the lower z_{\max} is found to have a significant effect. These findings are relevant in order to understand the well-known effect of inversions on poor air quality episodes. This is the

first study that separates the effect into the contributions from the inversion intensity and the multilayer inversions over Mexico City. The investigation of the seasonality and evolution of the quantities here (Γ_{\max} , Ri_B , θ , and θ_v profiles) may be useful for forecasting the duration and strength of poor air quality episodes.

Regarding the bulk Richardson number criterion, we find that the most unstable surface layers develop during the rainy season (June to October). Although, at higher levels, stable layers are present all year long, more layers with large Ri_B , and therefore with stable conditions, develop in winter. However, during spring, low Ri_B values at elevated levels (1–2 km) are found, indicating large instability due to intense vertical shear and little stratification.

Finally, it is clear that the thermal-stratification structure, and therefore the dynamical stability of the ABL in the Valley of Mexico, is very complex and it is able to stifle mixing processes, which, in turn, affects air quality. Therefore, further research on this stratification structure and its variability over the year is important for understanding both the physical mechanisms that give rise to the complex stratification as well as the possible effects that the topography may have on the multilayer thermal profiles. Additionally, radiosonde data of higher vertical resolution would help in representing the small-scale variations in the bulk Richardson number. Although radiosondes should have sufficiently high resolution (≈ 10 m), the long-term available radiosonde data considered here have coarser vertical resolution. The present investigation may be influential to understand long-term variability of pollutant concentrations by way of studying years with stronger or more frequent higher values of Γ_{\max} and relating them to poor air quality years. Finally, further research may consider expanding this city-scale stratification structures to wider mesoscale effects on air quality, for instance, the effect of larger-scale forcing (such as cold fronts and anticyclones) on the stratification structures in the ABL may be further investigated.

Acknowledgements We thank CONACyT (Consejo Nacional de Ciencia y Tecnología) for providing financial support to pursue the doctoral studies of A. Burgos., D. Adams thanks *Programa de Apoyos para la Superación del Personal Académico* (PASPA), UNAM for support during his sabbatical year at Rutgers, The State University of New Jersey during which this paper was written. We also thank all those who were responsible for radiosonde launching, air pollution measurements and data management in the SMN (*Servicio Meteorológico Nacional*) and the *Red Automática de Monitoreo Atmosférico* (RAMA). Finally, we express our gratitude for those who were always willing to help and contribute in the present research. In particular, thanks to Alejandro Jaramillo for his comments on the manuscript.

References

- Adler B, Kalthoff N (2014) Multi-scale transport processes observed in the boundary layer over a mountainous island. *Boundary-Layer Meteorol* 153(3):515–537
- Apel E, Emmons L, Karl T, Flocke F, Hills A, Madronich S, Lee-Taylor J, Fried A, Weibring P, Walega J et al (2010) Chemical evolution of volatile organic compounds in the outflow of the Mexico City Metropolitan area. *Atmos Chem Phys* 10(5):2353–2375
- Arduini G, Staquet C, Chemel C (2016) Interactions between the nighttime valley-wind system and a developing cold-air pool. *Boundary-Layer Meteorol* 161(1):49–72
- Badarinath K, Sharma AR, Kharol SK, Prasad VK (2009) Variations in CO, O₃ and black carbon aerosol mass concentrations associated with planetary boundary layer (PBL) over tropical urban environment in India. *J Atmos Chem* 62(1):73–86
- Barlow JF (2014) Progress in observing and modelling the urban boundary layer. *Urb Clim* 10:216–240
- Barrett BS, Raga GB (2016) Variability of winter and summer surface ozone in Mexico City on the intraseasonal timescale. *Atmos Chem Phys* 16(23):15,359–15,370
- Barrett BS, Fitzmaurice SJ, Pritchard SR (2012) Intraseasonal variability of surface ozone in Santiago, Chile: Modulation by phase of the Madden–Julian oscillation (MJO). *Atmos Environ* 57:55–62

- Berkes F, Hoor P, Bozem H, Kunkel D, Sprenger M, Henne S (2016) Airborne observation of mixing across the entrainment zone during PARADE 2011. *Atmos Chem Phys* 16(10):6011–6025
- Cao G, Giambelluca TW, Stevens DE, Schroeder TA (2007) Inversion variability in the Hawaiian trade wind regime. *J Clim* 20(7):1145–1160
- Carreón-Sierra S, Salcido A, Castro T, Celada-Murillo AT (2015) Cluster analysis of the wind events and seasonal wind circulation patterns in the Mexico City region. *Atmosphere* 6(8):1006–1031
- Chavez-Baeza C, Sheinbaum-Pardo C (2014) Sustainable passenger road transport scenarios to reduce fuel consumption, air pollutants and GHG (greenhouse gas) emissions in the Mexico City Metropolitan Area. *Energy* 66:624–634
- Cooper D, Eichinger W (1994) Structure of the atmosphere in an urban planetary boundary layer from lidar and radiosonde observations. *J Geophys Res Atmos* 99(D11):22,937–22,948
- Coulter RL (1979) A comparison of three methods for measuring mixing-layer height. *J Appl Meteorol* 18(11):1495–1499
- De Foy B, Zavala M, Bei N, Molina L (2009) Evaluation of WRF mesoscale simulations and particle trajectory analysis for the MILAGRO field campaign. *Atmos Chem Phys* 9:4419–4438
- De Wekker SF, Kossmann M (2015) Convective boundary layer heights over mountainous terrain—a review of concepts. *Front Earth Sci* 3:77
- Doran C (2007) The t1–t2 study: evolution of aerosol properties downwind of Mexico City. *Atmos Chem Phys* 7:2197–2198
- Doran JC, Abbott S, Archuleta J, Bian X, Chow J, Coulter R, De Wekker S, Edgerton S, Elliott S, Fernandez A (1998) The IMADA-AVER boundary layer experiment in the Mexico City area. *Bull Am Meteorol Soc* 79(11):2497–2508
- de Foy B, Clappier A, Molina L, Molina M (2006) Distinct wind convergence patterns in the Mexico City basin due to the interaction of the gap winds with the synoptic flow. *Atmos Chem Phys* 6(5):1249–1265
- García-Franco JL, Stremme W, Bezanilla A, Ruiz-Angulo A, Grutter M (2018) Variability of the mixed-layer height over Mexico City. *Boundary-Layer Meteorol* 167(3):493–507
- García-Franco JL (2020) Air quality in Mexico City during the fuel shortage of January 2019. *Atmos Environ* 222:117,131. <https://doi.org/10.1016/j.atmosenv.2019.117131>
- Garratt JR (1994) The atmospheric boundary layer. *Earth-Sci Rev* 37(1–2):89–134
- Gorham KA, Blake NJ, VanCuren RA, Fuelberg HE, Meinardi S, Blake DR (2010) Seasonal and diurnal measurements of carbon monoxide and nonmethane hydrocarbons at Mt. Wilson, California: indirect evidence of atomic Cl in the Los Angeles basin. *Atmos Environ* 44(19):2271–2279
- Guo J, Miao Y, Zhang Y, Liu H, Li Z, Zhang W, He J, Lou M, Yan Y, Bian L et al (2016) The climatology of planetary boundary layer height in China derived from radiosonde and reanalysis data. *Atmos Chem Phys* 16(20):13,309
- Guo JP, Zhang XY, Che HZ, Gong SL, An X, Cao CX, Guang J, Zhang H, Wang YQ, Zhang XC et al (2009) Correlation between PM concentrations and aerosol optical depth in eastern China. *Atmos Environ* 43(37):5876–5886
- Haikin N, Galanti E, Reisin T, Mahrer Y, Alpert P (2015) Inner structure of atmospheric inversion layers over Haifa Bay in the Eastern Mediterranean. *Boundary-Layer Meteorol* 156(3):471–487
- Hansen FV (1966) The Richardson number in the planetary boundary layer. Army electronics command white sands missile range NM Atmospheric Sciences Lab, Technical report
- Henne S, Furger M, Nyeki S, Steinbacher M, Neiningner B, De Wekker S, Dommen J, Spichtinger N, Stohl A, Prévôt A (2004) Quantification of topographic venting of boundary layer air to the free troposphere. *Atmos Chem Phys* 4(2):497–509
- Hennemuth B, Lammert A (2006) Determination of the atmospheric boundary layer height from radiosonde and lidar backscatter. *Boundary-Layer Meteorol* 120(1):181–200
- Herrera-Mejía L, Hoyos CD (2019) Characterization of the atmospheric boundary layer in a narrow tropical valley using remote-sensing and radiosonde observations and the WRF model: the Aburrá Valley case-study. *Q J R Meteorol Soc* 145(723):2641–2665
- Huang M, Gao Z, Miao S, Chen F, LeMone MA, Li J, Hu F, Wang L (2017) Estimate of boundary-layer depth over Beijing, China, using Doppler lidar data during SURF-2015. *Boundary-Layer Meteorol* 162(3):503–522
- Jáuregui E (1988) Local wind and air pollution interaction in the Mexico basin. *Atmósfera* 1(3):131–140
- Jáuregui E (1997) Heat island development in Mexico City. *Atmos Environ* 31(22):3821–3831
- Jáuregui E, Romales E (1996) Urban effects on convective precipitation in Mexico City. *Atmos Environ* 30(20):3383–3389
- Jazcilevich AD, García AR, Ruíz-Suárez LG (2003) A study of air flow patterns affecting pollutant concentrations in the Central Region of Mexico. *Atmos Environ* 37(2):183–193
- Kampa M, Castanas E (2008) Human health effects of air pollution. *Environ Pollut* 151(2):362–367

- Kolev I, Savov P, Kaprielov B, Parvanov O, Simeonov V (2000) Lidar observation of the nocturnal boundary layer formation over Sofia, Bulgaria. *Atmos Environ* 34(19):3223–3235
- Largeroy Y, Staquet C (2016a) The atmospheric boundary layer during wintertime persistent inversions in the Grenoble valleys. *Front Earth Sci* 4:70
- Largeroy Y, Staquet C (2016b) Persistent inversion dynamics and wintertime PM10 air pollution in Alpine valleys. *Atmos Environ* 135:92–108
- LeMone MA, Tewari M, Chen F, Dudhia J (2013) Objectively determined fair-weather CBL depths in the ARW-WRF model and their comparison to CASES-97 observations. *Mon Weather Rev* 141(1):30–54
- LeMone MA, Tewari M, Chen F, Dudhia J (2014) Objectively determined fair-weather NBL features in ARW-WRF and their comparison to CASES-97 observations. *Mon Weather Rev* 142(8):2709–2732
- Levi Y, Dayan U, Levy I, Broday DM et al (2020) On the association between characteristics of the atmospheric boundary layer and air pollution concentrations. *Atmos Res* 231(104):675
- Li Z, Guo J, Ding A, Liao H, Liu J, Sun Y, Wang T, Xue H, Zhang H, Zhu B (2017) Aerosol and boundary-layer interactions and impact on air quality. *Natl Sci Rev* 4:810–833
- Mahrt L (1999) Stratified atmospheric boundary layers. *Boundary-Layer Meteorol* 90(3):375–396
- Martilli A (2007) Current research and future challenges in urban mesoscale modelling. *Int J Climatol Atmos J R Meteorol Soc* 27(14):1909–1918
- Martucci G, Matthey R, Mitev V, Richner H (2007) Comparison between backscatter lidar and radiosonde measurements of the diurnal and nocturnal stratification in the lower troposphere. *J Atmos Ocean Technol* 24(7):1231–1244
- Molina L, Kolb C, De Foy B, Lamb B, Brune WH, Jimenez J, Molina M (2007) Air quality in North America's most populous city overview of MCMA-2003 campaign. *Eur Geosci Union* 14:2447–2473
- Molina LT, Madronich S, Gaffney J, Apel E, Foy Bd, Fast J, Ferrare R, Herndon S, Jimenez JL, Lamb B et al (2010) An overview of the MILAGRO 2006 Campaign: Mexico City emissions and their transport and transformation. *Atmos Chem Phys* 10(18):8697–8760
- Molina LT, Lei W, Zavala M, Almanza V, Garcia A, Saide P, Mena-Carrasco M (2018) Atmospheric pollution: Experience from Mexico City and Santiago de Chile. In: International technical meeting on air pollution modelling and its application, Springer, pp 127–138
- Naakka T, Nygård T, Vihma T (2018) Arctic humidity inversions: climatology and processes. *J Clim* 31(10):3765–3787
- Nodzu MI, Ogino SY, Tachibana Y, Yamanaka MD (2006) Climatological description of seasonal variations in lower-tropospheric temperature inversion layers over the Indochina Peninsula. *J Clim* 19(13):3307–3319
- Oke T, Zeuner G, Jauregui E (1992) The surface energy balance in Mexico City. *Atmos Environ Part B Urban Atmos* 26(4):433–444
- Ortuño C, Jaimes M, Muñoz R, Ramos R, Paramo VH (1997) Redundancy analysis for the Mexico City air monitoring network: the case of CO. In: Proceedings of the air and waste management association's annual conference and exhibition, , vol 2. <http://files.abstractonline.com/CTRLD>
- Pal S, Haefelin M (2015) Forcing mechanisms governing diurnal, seasonal, and interannual variability in the boundary layer depths: five years of continuous lidar observations over a suburban site near Paris. *J Geophys Res Atmos* 120(23):11–936
- Peralta O, Ortíz-Alvarez A, Basaldud R, Santiago N, Alvarez-Ospina H, de la Cruz K, Barrera V, de la Luz Espinosa M, Saavedra I, Castro T, Martínez-Arroyo A, Páramo VH, Ruíz-Suárez LG, Vázquez-Galvez FA, Gavián A (2019) Atmospheric black carbon concentrations in Mexico. *Atmos Res* 230:104,626. <https://doi.org/10.1016/j.atmosres.2019.104626>
- Quan J, Gao Y, Zhang Q, Tie X, Cao J, Han S, Meng J, Chen P, Zhao D (2013) Evolution of planetary boundary layer under different weather conditions, and its impact on aerosol concentrations. *Particuology* 11(1):34–40
- Raga G, Le Moine L (1996) On the nature of air pollution dynamics in Mexico City—I. Nonlinear analysis. *Atmos Environ* 30(23):3987–3993
- Raga G, Castro T, Baumgardner D (2001) The impact of megacity pollution on local climate and implications for the regional environment: Mexico City. *Atmos Environ* 35(10):1805–1811
- Ragsdale KM, Barrett BS, Testino AP (2013) Variability of particulate matter (PM10) in Santiago, Chile by phase of the Madden-Julian Oscillation (MJO). *Atmos Environ* 81:304–310
- Retama A, Baumgardner D, Raga G, McMeeking G, Walker J (2015) Seasonal and diurnal trends in black carbon properties and co-pollutants in Mexico City. *Atmos Chem Phys* 15(16):9693
- Serafin S, Adler B, Cuxart J, De Wekker SF, Gohm A, Grisogono B, Kalthoff N, Kirshbaum DJ, Rotach MW, Schmidli J et al (2018) Exchange processes in the atmospheric boundary layer over mountainous terrain. *Atmosphere* 9(3):102
- Steyn DG, Baldi M, Hoff R (1999) The detection of mixed layer depth and entrainment zone thickness from lidar backscatter profiles. *J Atmos Ocean Technol* 16(7):953–959

- Stull RB (2012) An introduction to boundary layer meteorology, vol 13. Springer, Berlin
- Sun J, Mahrt L, Nappo C, Lenschow DH (2015) Wind and temperature oscillations generated by wave–turbulence interactions in the stably stratified boundary layer. *J Atmos Sci* 72(4):1484–1503
- Tiwari S, Srivastava A, Bisht D, Parmita P, Srivastava MK, Attri S (2013) Diurnal and seasonal variations of black carbon and PM_{2.5} over New Delhi, India: influence of meteorology. *Atmos Res* 125:50–62
- Van Pul W, Holtslag A, Swart D (1994) A comparison of ABL heights inferred routinely from lidar and radiosondes at noontime. *Boundary-Layer Meteorol* 68(1–2):173–191
- Velasco E, Márquez C, Bueno E, Bernabé R, Sánchez A, Fentanes O, Wöhrnschimmel H, Cárdenas B, Kamilla A, Wakamatsu S et al (2008) Vertical distribution of ozone and VOCs in the low boundary layer of Mexico City. *Atmos Chem Phys* 8(12):3061–3079
- Wang T, Cheung VT, Anson M, Li Y (2001) Ozone and related gaseous pollutants in the boundary layer of eastern China: overview of the recent measurements at a rural site. *Geophys Res Lett* 28(12):2373–2376
- Wang Y, Ying Q, Hu J, Zhang H (2014) Spatial and temporal variations of six criteria air pollutants in 31 provincial capital cities in China during 2013–2014. *Environ Int* 73:413–422
- Whiteman C, Zhong S, Bian X, Fast J, Doran J (2000) Boundary layer evolution and regional-scale diurnal circulations over the and Mexican plateau. *J Geophys Res Atmos* 105(D8):10081–10102
- Whiteman CD, Bian X, Zhong S (1999) Wintertime evolution of the temperature inversion in the Colorado Plateau Basin. *J Appl Meteorol* 38(8):1103–1117
- Zhang H, Wang Y, Hu J, Ying Q, Hu XM (2015) Relationships between meteorological parameters and criteria air pollutants in three megacities in China. *Environ Res* 140:242–254
- Zhang W, Guo J, Miao Y, Liu H, Song Y, Fang Z, He J, Lou M, Yan Y, Li Y et al (2018) On the summertime planetary boundary layer with different thermodynamic stability in China: a radiosonde perspective. *J Clim* 31(4):1451–1465
- Zhang Y, Dubey M, Olsen S, Zheng J, Zhang R (2009) Comparisons of WRF/Chem simulations in Mexico City with ground-based RAMA measurements during the 2006-MILAGRO. *Atmos Chem Phys* 9(11):3777–3798
- Zhang Y, Gao Z, Li D, Li Y, Zhang N, Zhao X, Chen J (2014) On the computation of planetary boundary-layer height using the bulk Richardson number method. *Geosci Model Dev* 7(6):2599–2611
- Zhao S, Yu Y, Yin D, Qin D, He J, Dong L (2018) Spatial patterns and temporal variations of six criteria air pollutants during 2015 to 2017 in the city clusters of Sichuan Basin, China. *Sci Total Environ* 624:540–557
- Zhou B, Lauwaet D, Hooyberghs H, De Ridder K, Kropp JP, Rybski D (2016) Assessing seasonality in the surface urban heat island of London. *J Appl Meteorol Climatol* 55(3):493–505

Publisher's Note Springer Nature remains neutral with regard to jurisdictional claims in published maps and institutional affiliations.